Volume 10
Number 1
January 2023
Pages 1–278

Materials Horizons

rsc.li/materials-horizons

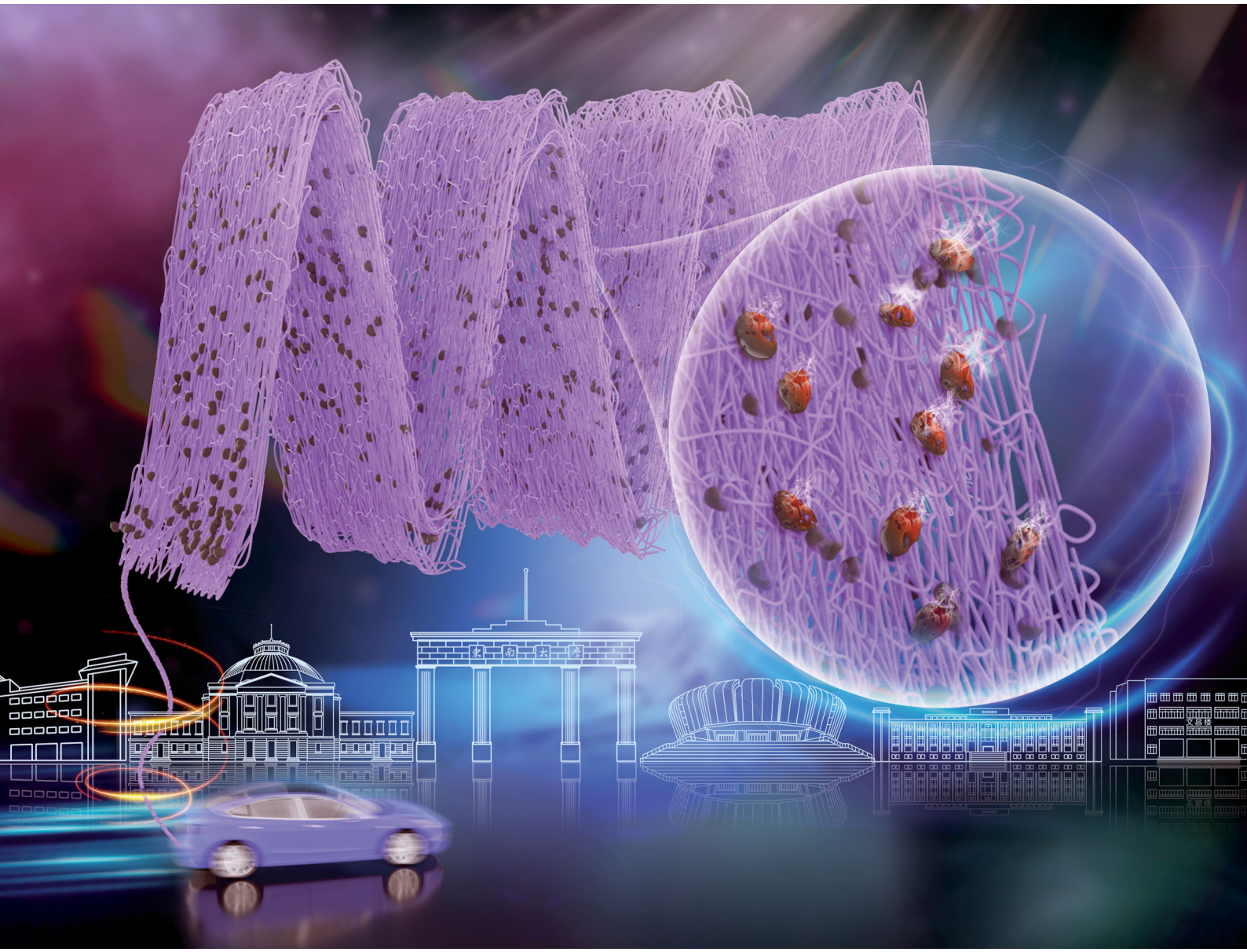

ISSN 2051-6347

ROYAL SOCIETY OF CHEMISTRY

COMMUNICATION

Yunqian Dai *et al.*

Flexible-in-rigid polycrystalline titanium nanofibers: a toughening strategy from a macro-scale to a molecular-scale

Materials Horizons

ROYAL SOCIETY OF CHEMISTRY

COMMUNICATION

View Article Online
View Journal | View Issue

Cite this: *Mater. Horiz.*, 2023, 10, 65

Received 9th October 2022,
Accepted 23rd November 2022

DOI: 10.1039/d2mh01255c

rsc.li/materials-horizons

Flexible-in-rigid polycrystalline titanium nanofibers: a toughening strategy from a macro-scale to a molecular-scale†

Wanlin Fu, ‡[a] Wanlin Xu,‡[a] Kuibo Yin, ‡[b] Xiangyu Meng, [a] Yujie Wen,[c] Luming Peng, [c] Mingyu Tang,[a] Litao Sun, [b] Yueming Sun[a] and Yunqian Dai *[a]

TiO_2 nanomaterials, especially one-dimensional TiO_2 nanofibers fabricated by electrospinning, have received considerable attention in the past two decades, for a variety of basic applications. However, their safe use and easy recycling are still hampered by the inherently subpar mechanical performance. Here, we toughened polycrystalline TiO_2 nanofibers by introducing Al^{3+}-species at the very beginning of electrospinning. The resultant long-and-continuous TiO_2 nanofibers achieved a Young's modulus of 653.8 MPa, which is *ca.* 25-fold higher than that of conventional TiO_2 nanofibers. Within each nanofiber, amorphous Al_2O_3-based oxide effectively hindered the coalescence of TiO_2 nanocrystals and potentially repaired the surface groves. The solid-state ^{17}O-NMR spectra further revealed the toughening strategy on a molecular scale, where relatively flexible Ti–O–Al bonds replaced rigid O–Ti–O bonds at the interfaces of TiO_2 and Al_2O_3. Moreover, the modified TiO_2 nanofibers exhibited superb sinter-resistance, without cracking over 900 °C, which was dynamically monitored by TEM. Therefore, flexible-in-rigid TiO_2 fibrous mats can be facilely folded into 3D sponges through origami art. As a potential showcase, the TiO_2 sponges were demonstrated as a duarable and renewable filtrator with a high filtration efficiency of 99.97% toward $PM_{2.5}$ and 99.99% toward PM_{10} after working for 300 min. This work provides a rational strategy to produce flexible oxide nanofibers and gives an in-depth understanding of the toughening mechanism from the macro-scale to the molecular-scale.

New concepts

This research offers a fresh concept and a thorough understanding of how to toughen electrospun TiO_2 nanofibers from the macro to the molecular scales. A combination of finite element analysis and structure observations revealed that TiO_2 nanofibers can be effectively reinforced by promoting the length–diameter ratio, restricting crystal size, and repairing surface grooves. At the interfaces of neighboring nanocrystals, an amorphous solid solution can serve as a lubrication zone, dissipating the localized stress. More inherently, the replacement of rigid Ti–O–Ti bonds by relatively soft Ti–O–Al bonds allows various deformations including twisting, switching, and vibration. The *in situ* heating TEM observation further showcased the superb sinter-resistance of the modified TiO_2 nanofibers, avoiding undesirable thermal-stress-induced break into short segments. By taking advantage of the origami craft, such thermally stable, flame resistant, and mechanically strong fibrous mats can be engineered into 3D sponges, holding broad application promise, such as renewable air filters. It therefore demonstrates a proof-of-concept for the continuous and controlled production of flexible oxide nanofibers, hastening the transition of TiO_2-based nanomaterials from the fab to the lab.

Introduction

Titanium dioxide (TiO_2) has attracted much attention and is widely used in the photocatalytic degradation of pollutants,[1] photocatalytic CO_2/CH_4 conversion into energy fuels,[2] water splitting,[3] and solar cells.[4] Its global market size is expected to reach USD 26.87 billion by 2028 and its compound annual growth rate was forecast to be as high as 6.0% from 2021 to 2028.[5] Compared with conventionally explored powder TiO_2 materials, one-dimensional (1D) TiO_2 nanostructures featuring distinctive chemical and physical properties offered new opportunities for the scientific community and industry.[6] In specific, the millimeter length scale together with the nanometer diameter scale of TiO_2 nanofibers allows them to connect the macroscopic world with nanoscience and nanotechnology. Since the first report of electrospun TiO_2 nanofibers in 2003,[7] a number of TiO_2-based nanofibers have been elegantly and

[a] *School of Chemistry and Chemical Engineering, Southeast University, Nanjing, Jiangsu, 211189, P. R. China. E-mail: daiy@seu.edu.cn*
[b] *SEU-FEI Nano-Pico Center, Key Laboratory of MEMS of Ministry of Education, School of Electronic Science and Engineering, Southeast University, Nanjing, Jiangsu, 211189, P. R. China*
[c] *Key Laboratory of Mesoscopic Chemistry of Ministry of Education, School of Chemistry and Chemical Engineering, Nanjing University, Nanjing, 210023, China*

† Electronic supplementary information (ESI) available. See DOI: https://doi.org/10.1039/d2mh01255c

‡ These three authors contributed equally to this work.

continuously produced through electrospinning, and have shown great potential in energy conversion and environmental governance in the past two decades.[8,9] However, these carefully prepared TiO_2 nanofibers generally suffered from breaking into short segments and therefore lost all the merits arising from the 1D nanostructure, during use and/or fabrication.

On a nano-scale, low dimension and small size result in a lower melting point and higher surface energy for TiO_2 nanofibers, in comparison with those for the bulk TiO_2 counterparts. Therefore, TiO_2 nanocrystallites, the building block for each nanofiber, would severely sinter during the indispensable heat treatment, despite high crystallinity and the corresponding (photo)catalytic activities. In this case, macrogrooves can form on the bamboo-like nanofiber surface and propagate along the grain boundaries quickly under external loading.[10] On a molecular scale, the firm and solid ionic bonds make TiO_2 inherently brittle in shearing and tension,[11] being quite different from the recently demonstrated flexible SiO_2 nanofibers featuring an amorphous nature.[12] Generally, the continuous random network of Si–O–Si bonds has multitudinous angles ranging from 120° to 180°. As a result, the switchable bond lengths and bond angles in silicon oxygen tetrahedra endow a single SiO_2 nanofiber with surprising flexibility.[12] However, it is still a challenging task yet fascinating to produce flexible nanofibers composed of robust and polycrystalline TiO_2, and some other functional oxides with low crystalline temperatures, such as ZrO_2, Fe_2O_3, ZnO, and CeO_2.

One recent research study demonstrated that the structural resilience of ZrO_2 nanofibers can be optimized by embedding ZrO_2 nanocrystallites into an amorphous zircon matrix.[13] Upon loading, the relatively flexible zircon would lubricate the brittle ZrO_2 nanocrystallites and allow more deformations to dispersive stress. As an alternative tactic, the grain growth in oxide nanofibers can be effectively hampered by coating an Al_2O_3 shell outside the surface *via* co-axial electrospinning, therefore enhancing their thermal and mechanical stability.[10] Indeed, coating soft materials outside each oxide nanocrystal or individual nanofiber is a valid protocol to improve the elasticity and toughness, but will be achieved with a sacrifice of the functional surfaces of nanocrystallites with an ideal crystalline structure more or less. Therefore, boosting the intrinsic strength and toughness of oxide nanofibers while retaining functionality is still an exciting and unattained goal.

Herein, we demonstrate a facile strategy to reinforce polycrystalline TiO_2 nanofibers from a macro-scale to a molecular-scale, by introducing Al^{3+}-species at the very beginning of electrospinning. The resultant modified TiO_2 nanofibers were endowed with restricted crystal size, repaired surface grooves, lubricated interstitial regions, and a high length-to-diameter ratio, and hence achieved an optimized tensile breaking strength of 2.24 MPa, being one of the strongest TiO_2-based fibrous mats rarely demonstrated. Moreover, the flexible-in-rigid TiO_2-based nanofibers exhibited superb sinter-resistance over 900 °C, which was dynamically revealed by *in situ* TEM observation. Due to the remarkable flexibility, thermal stability, flame resistance, and (photo)catalytic activity, the modified TiO_2-based nanofibers offered new opportunities for renewable air filters in a safe and cost-effective manner.

Results and discussion

Fabrication of flexible-in-rigid TiO_2 nanofibers

Electrospinning is an electrohydrodynamic technique in which a liquid droplet is electrified to form a jet, which is then stretched and elongated to form nanofibers. The jet solidifies quickly when it is stretched to smaller dimensions, resulting in the deposition of solid nanofibers on the grounded collector.[14] One great concern disturbing the integrity of the as-spun fibrous mat is to keep a balance between the rates of volatilization and nanofiber deposition. As illustrated in Fig. 1a and b, preserving sufficient solvent can help cross-link nanofibers, thus assuring good integrity of the as-spun fibrous mat without cracking, and also making it possible to obtain large-scale and self-supporting oxide fibrous mats even after the necessary heat-treatment. On the contrary, the as-spun fibrous mat would suffer from severe fracture when the deposition speed is too slow or the solvent evaporation/solidification process is too quick. Therefore, accelerating the nanofiber deposition with the aid of multiple-needle electrospinning becomes a promising protocol. Remarkably, the finite element simulation for the distribution of electric field during single-needle and multiple-needle electrospinning demonstrates that there is no charge accumulation in both the two modes (Fig. 1c). As schemed in Fig. 1d, we upgraded the electrospinning setup by employing an array of three-needle spinnerets and adding a cyclic reciprocating device to help deposit nanofibers fast and uniformly on the collector surface.

Commonly, TiO_2 nanofibers can be facilely fabricated by electrospinning a homogenous precursor containing polyvinylpyrrolidone (PVP), titanium isopropoxide (TTIP), ethanol, and acetic acid, followed by calcination in the air over 500 °C (Fig. S1, ESI†). In the precursor solution, Ti^{4+} serves as coordination centers to build stable Ti–O–Ti networks, in the form of $Ti(OR)_x{\cdot}(CH_3COO)_{4-x}$. Once the electrospinning process begins, the homogeneous sol is stretched into nanofibers, along with solvent evaporation and solidification. However, after the indispensable calcination over 500 °C, which is aimed at removing the polymer matrix and converting metal-salt to metal-oxide with the ideal phase, the resulting mat becomes extremely fragile and even difficult to be handled (Fig. S1a, ESI†). The representative TEM image in Fig. S1b (ESI†) gives more detailed information to understand the brittle nature of pristine TiO_2 nanofibers. As shown, a bamboo-like morphology can be observed, with distinctive surface grooves. Upon external loading, the surface grooves will serve as dislocation sources where the dislocations pile up, and a crack first appears, and then propagates along the grain boundaries.[15] As a result, continuous nanofibers as long as several hundreds of micrometers break into short segments (several micrometers) and the integrated fibrous mat generally suffers from undesirable fragility.

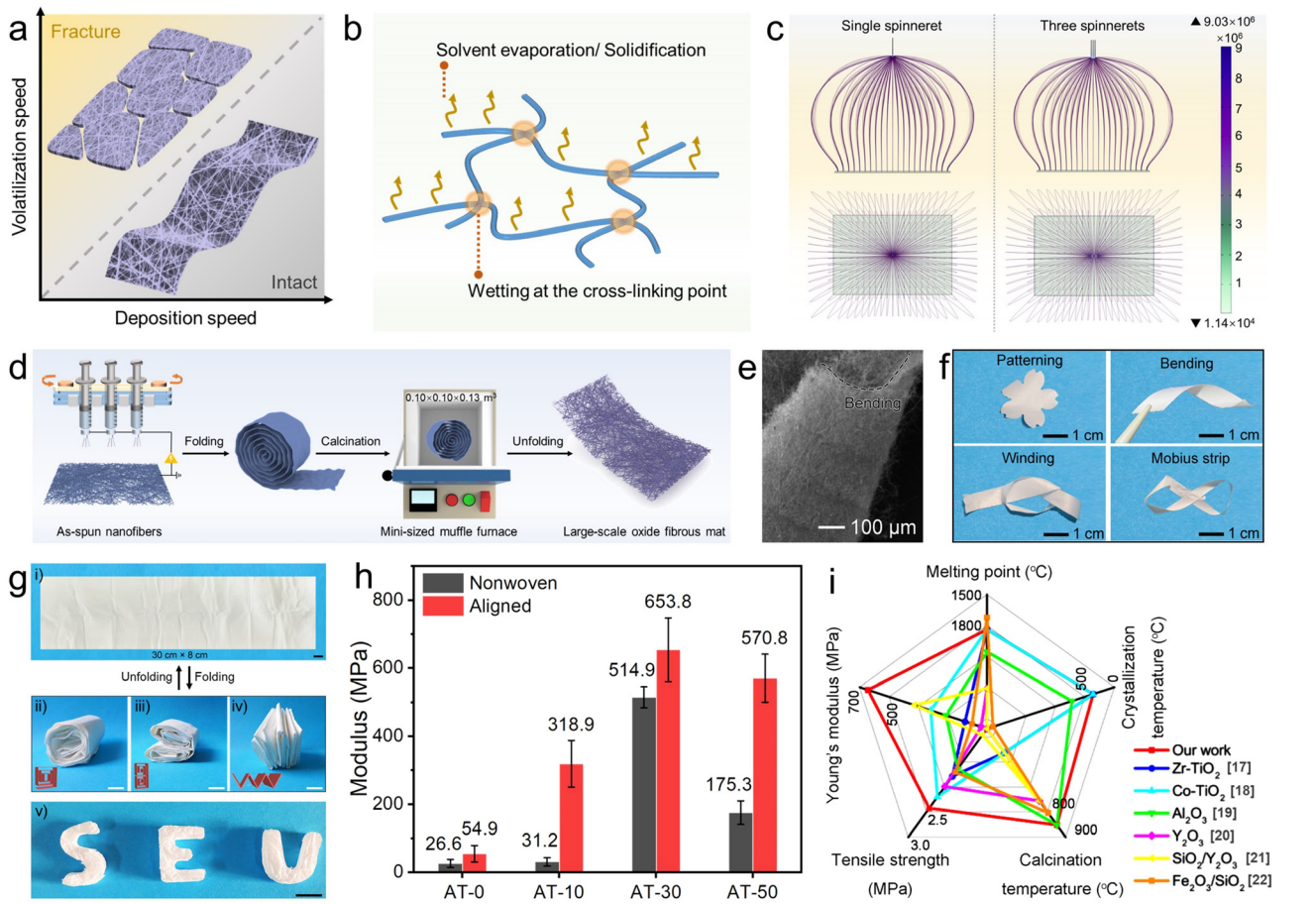

Fig. 1 (a) Integrity of the as-spun fibrous mat with regard to the balance of the rates of volatilization and the nanofibers deposition. (b) Scheme of the simultaneous solvent evaporation and the wetting at the cross-linking point within the as-spun nanofibers. (c) Simulation of the electric field lines during electrospinning with single and multiple needles. (d) Schematic illustration for the preparation of flexible-in-rigid TiO_2-based nanofibers (denoted as AT-*n* nanofibers). (e) SEM image of the bent AT-30 fibrous mat calcined at 900 °C. (f) Optical images of the AT-30 fibrous mat after patterning, bending, winding, and twisting. (g) Optical images of large-scale AT-30 fibrous mats before and after folding as layer-by-layer structures and 3D sponges with the aid of origami art. The scale bars in g represent 1 cm. (h) Young's modulus of AT-*n* fibrous mats. (i) Comparison of the physiochemical properties of AT fibrous mats and recently reported oxide fibrous mats.

When $Al(acac)_3$ and acetone were introduced into the electrospinning precursor, a stable sol of metal–organic groups bridged by O (*i.e.*, CH_3COO–Ti–O–Al–···–Ti–$OOCCH_3$) was formed. In each composing unit of Ti–O–Al, oxygen links Ti and Al atoms steadily and allows more deformation of chemical bonds in the forms of vibration, rotation, and distortion. Therefore, flexible-in-rigid TiO_2-based fibrous mats could be surprisingly obtained after calcination at temperatures ranging from 500 to 900 °C at least. The resultant nanofibers were denoted as AT-*n*, where *n* represents the atomic dosing percentage of Al to Ti.

As shown in the SEM image (Fig. 1e), the resultant AT-30 fibrous mat after calcination at 900 °C could withstand severe bending to a radius below 100 μm. Furthermore, the flexible-in-rigid AT-30 fibrous mats preserved their structural integrity even after being deformed in a variety of ways, such as patterning, bending, winding, and folding, with no distinctive crack (Fig. 1f). Due to the remarkable flexibility, large-scale TiO_2-based fibrous mats (determined from the size of the collector only) can be easily fabricated by folding the as-spun composite fibrous mat into a roll and keeping it in a mini-sized muffle furnace ($0.10 \times 0.10 \times 0.13$ m^3) to be calcined at a given temperature, as schemed in Fig. 1d. The obtained TiO_2 fibrous mat could be unfolded into a flat and intact mat, and then refolded into various shapes repeatedly (Fig. 1g and Video S1, ESI†). Such an elegant protocol opens a brand-new avenue for scaling-up the production of oxide fibrous mats and breaks the limitations imposed by the space of muffle furnaces for the unavoidable calcination processes.

Although oxide nanofibrous sponges offer exceptional qualities such as high porosity, large surface areas, outstanding flame resistance, and thermal-insulation ability, the construction of three-dimensional (3D) oxide nanofibrous sponges without binders and templates is still difficult because of the brittleness and defect sensitivity of the building block, *i.e.*, individual oxide nanofibers. Due to the remarkable flexibility and foldability, the AT fibrous mat could be easily constructed into 3D sponges by simply combining

with origami craft, achieving an average density of only 22 mg cm^{-3} (Fig. 1g and Video S2, ESI†). Such an ultralow density is even lower than that of recently demonstrated TiO_2 aerogels.[16] Moreover, the oxide nature allows the sponge to feature superb flame retarding ability and thermal insulation at a high temperature of 1300 °C (Fig. S2 and Video S3, S4, ESI†).

For a more intuitive understanding of the mechanical performance of the TiO_2-based nanofibers, tensile stress–strain tests were conducted on a series of fibrous mats. As shown in Fig. 1h and Fig. S3 (ESI†), Young's modulus increased strikingly from 26.6 MPa for nonwoven traditional TiO_2 fibrous mats to 514.9 MPa for nonwoven AT-30 fibrous mats, and then declined to 176.3 MPa for AT-30 nonwoven fibrous mats. To further improve the mechanical performance, we simply aligned the nanofibers by applying a drum collector with a rotation speed of 1500 rpm during electrospinning (Fig. S4, ESI†). As expected, Young's modulus of the nonwoven AT-30 fibrous mat was highly improved to 653.8 MPa after being aligned. This optimization should be ascribed to the high orientation of nanofibers along with macroscopic and molecular arrays, which increases the fracture resistance under the effects of high-speed stretching. Compared with previous reports (Fig. 1i),[17–22] the resultant fibrous mats exhibited superior mechanical strength. Specifically, the tensile breaking strength of aligned AT-30 nanofibers reached to 2.24 MPa, making them the strongest TiO_2-based fibrous mat ever achieved. Moreover, the Young's modulus of the aligned AT-30 fibrous mat is 2-times higher than that of the SiO_2 fibrous mat (calcined at 900 °C).

Toughening strategy on a macro-scale

On a macro-scale, the length–diameter ratio plays a significant role in the mechanical performance of fibrous mats. For a deeper understanding, we simulated the stress distribution on individual nanofibers (300 nm in diameter) with different length–diameter ratios, *i.e.*, 5 : 1 and 25 : 1, respectively, as shown in Fig. 2a. During finite element analysis, the vertical upward force was applied along the *z*-axis direction. There is no doubt that the flexibility could be highly improved by increasing the length–diameter ratio, instead of breaking it into short segments. Accordingly, the typical SEM image of unmodified TiO_2 nanofibers evidenced the cracks after harsh aging at 900 °C. After incorporating a handful of Al_2O_3-based species, the continuity of AT nanofibers improved greatly, thereby enhancing the good integrity of the resultant fibrous mats.

Toughening strategy on a nano-scale

On a nano-scale, the pore structure, including surface grooves (volumetric defects located on or adjacent to the surface) and internal defects, is a key factor determining the mechanical performance of nanomaterials.[23] Cracks were observed to initiate and then propagate along the surface micro-notches and the internal defects. As simulated (Fig. 2b), the loaded stress was highly localized on the surface notch, while the nanofiber without surface defects had a considerably more uniform stress dispersion. The SEM images of one individual nanofiber gave strong evidence that the surface of the modified nanofibers was surprisingly decorated with abundant heterojunctions, which somewhat tended to remain and "fill" the surface grooves, and therefore accounted for the improved mechanical performance.

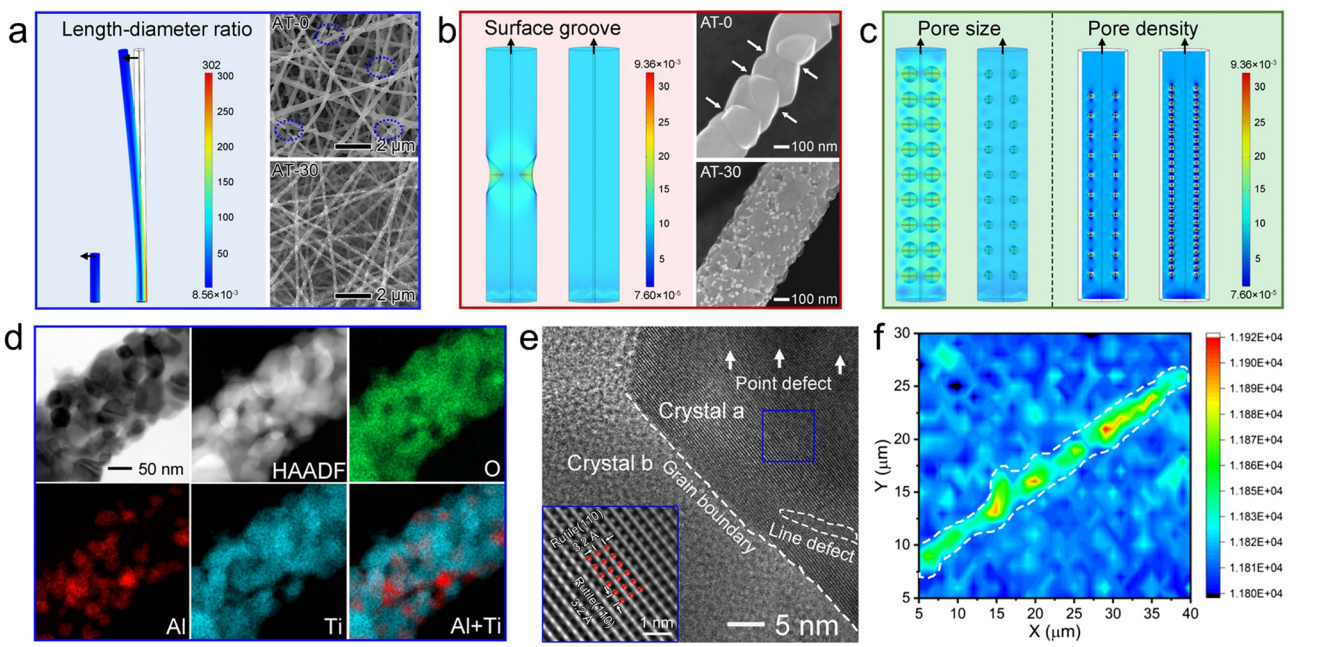

Fig. 2 (a–c) Finite element analysis at a single-nanofiber level for the stress distribution with different (a) length–diameter ratios, (b) surface defect structures, (c) pore sizes and pore densities, upon external loading (indicated by the black arrows). The insets in a and b show the SEM images of AT-0 and AT-30 fibrous mats and individual nanofibers calcined at 900 °C. (d) TEM, HAADF-STEM images, corresponding elemental mappings, (e) HRTEM image, and (f) Raman mapping along with the E_g (144 cm^{-1}) direction of one individual AT-30 nanofiber calcined at 900 °C.

Besides, in order to reveal the impact of internal pores within nanofibers on the mechanical performance, we conducted simulations of stress distribution on nanofibers with different pore sizes and densities (Fig. 2c). As shown, the nanofibers with restricted small pore size and high pore density could maintain homogeneous dispersion of loaded stress. Nitrogen physisorption isotherms give initial evidence of the enriched internal pores in the AT blended nanofibers with increasing Al_2O_3-based species (Fig. S5, ESI†). In the low relative pressure ranges ($P/P_0 < 0.9$), the nitrogen adsorption content of AT-*n* increased with the increasing atomic ratio of Al to Ti. Additionally, the AT-30 and AT-50 nanofibers showed higher hysteresis loop effects than the AT-10 and AT-0 nanofibers. As summarized in Fig. S5b (ESI†), the pore volume increased strikingly from 0 to 0.0045, 0.020, and 0.072 $cm^3\ g^{-1}$, when the atomic ratio of Al to Ti increased from 0 to 50%. Taking the theoretical density of these samples (4.1 $g\ cm^{-3}$) into consideration, the raw porosities of AT-0, AT-10, AT-30, and AT-50 can be calculated as 0, 1.89%, 8.20%, and 28.7%, respectively. As shown in Fig. S5c (ESI†), on increasing the porosity from 0 to 8.20%, the mechanical strength increased gradually. But a further increase in the porosity resulted in a decline of Young's modulus.

On the other hand, decreasing the crystal size could decentralize the loaded tension on abundant nanocrystals and restrict the stress-induced crevice propagation along the grain boundaries, which is known as the Hall–Petch effect.[24] Both the TEM images (Fig. 2d and Fig. S1b, ESI†) and XRD patterns (Fig. S6, ESI†) clearly confirmed that the sintering of TiO_2 nanocrystals can be finely suppressed by introducing Al_2O_3-based oxide. According to the Scherrer formula,[25] the crystal size can be estimated based on the most intensive peak. It is shown that the crystal size of AT-10, AT-30, and AT-50 declined to 22.4, 22.1, and 31.1 nm, respectively, from 60.2 nm in the unmodified TiO_2 nanofibers. No characteristic diffraction peak indexed to Al_2O_3 or Al_2O_3–TiO_2 solid solution could be observed, indicating their amorphous nature and/or high dispersity. More intriguingly, 47.0% anatase was observed in AT-30 blended nanofibers at temperatures up to 900 °C (Fig. S6c, ESI†), despite the fact that the phase transition from anatase to thermodynamically favorable rutile commonly starts at 600 °C. Considering that a mixture of anatase and rutile confers higher activity for photocatalytic applications,[26] the AT blended nanofibers offer significant potential in broad fields of energy conversion and environmental remediation.

As shown in a representative HRTEM image (Fig. 2e), the rutile phase of nanocrystals can be identified from the distinct fringes with a lattice distance of 3.2 Å, which are ascribed to the (110) facet. Within the nanocrystals, there were plentiful point defects and line defects. These long-range-disordered areas were insensitive to rupture, and thus allowed high elastic strain in the forms of the elastic elongation of bonds and changes in the bond-angle distribution. The crystallinity and grain boundaries were further assessed using a Raman spectral map (Fig. 2f and Fig. S7, ESI†). As seen in the map plotted along the E_g (144 cm^{-1}) direction, the crystallinity of the grains at the center of one nanofiber is obviously higher than that on the surface or at the grain boundaries. This can be understood by taking into consideration the directional distribution of amorphous oxide and solid solution on the surface of nanofibers and at the grain boundaries. Therefore, these soft oxides would lubricate the adjacent TiO_2 nanocrystals and allow more deformations upon loading.

Taken together, it was reasonable to deduce that small crystal size and intricate grain boundaries lacking interstitial pores could scatter and dissipate the stress concentration on a large scale, when bending the nanofiber *via* microscale movements, which greatly contributed to the high mechanical stability. However, excessive porosity results in loose stacking of the nanocrystals within each individual nanofiber, making the fibers susceptible to breaking under external force, despite a small crystal size.

Toughening strategy on a molecular-scale

To shed light on the toughening mechanism on a molecular scale, the coordination environments of Al^{3+} and Ti^{4+} were further investigated using X-ray photoelectron spectroscopy (XPS) spectra (Fig. 3a and b). As shown in Fig. 3a, partially reduced Ti^{3+} and Ti^{2+} can be surprisingly observed on AT-30 nanofibers, which is in clear contrast to the observation on pure TiO_2 nanofibers. When the Al/Ti atomic ratio was further increased to 30%, the Ti^{3+} peaks disappeared, leaving Ti^{2+} and Ti^{4+} peaks only. Such a partial reduction of Ti^{4+} in an oxygen-rich atmosphere can be somewhat ascribed to Al^{n+} doping, through which the Al^{n+} ions entered the TiO_2 lattice and replaced the lattice oxygen. More intriguingly, a binding energy of 76.4 eV was visualized in the AT-30 and AT-50 nanofibers, which should be indexed to the Al–O–Ti bonds.

Fig. 3c shows the solid-state ^{17}O-nuclear magnetic resonance (NMR) spectra of AT-30 blended nanofibers, along with those of pure Al_2O_3 nanofibers and pure TiO_2 nanofibers as references. The characteristic ranges of the chemical shifts corresponded with various coordination environments of O^{2-} because the ^{17}O resonance is mainly determined from its neighboring anions. The characteristic shift at around 350 ppm was a clear indication of the presence of Al–O–Ti in the AT blended nanofibers. These results strongly verified the formation of an Al_2O_3–TiO_2 solid solution.

As illustrated in Fig. 3d, the replacement of rigid Ti–O bonds with a vibrational energy of 503 kJ mol^{-1} with soft Al–O bonds with a lower vibrational energy of 488 kJ mol^{-1} can lead to toughening of the TiO_2-based nanofibers intrinsically.[27] In the blended nanofibers, the multifarious bonds with different lengths and angles allow various molecular-scale deformations, including rotation, twist, and vibration upon loading, and can thereby significantly decentralize the local stress.

Dynamic observation of the sinter-resistance of TiO_2-based nanofibers

In addition to mechanical stress, thermal stress is another important external stimulus affecting the structural stability of nanomaterials. For exploring the sinter-resistance, one representative AT-30 nanofiber (pre-calcined at 700 °C in

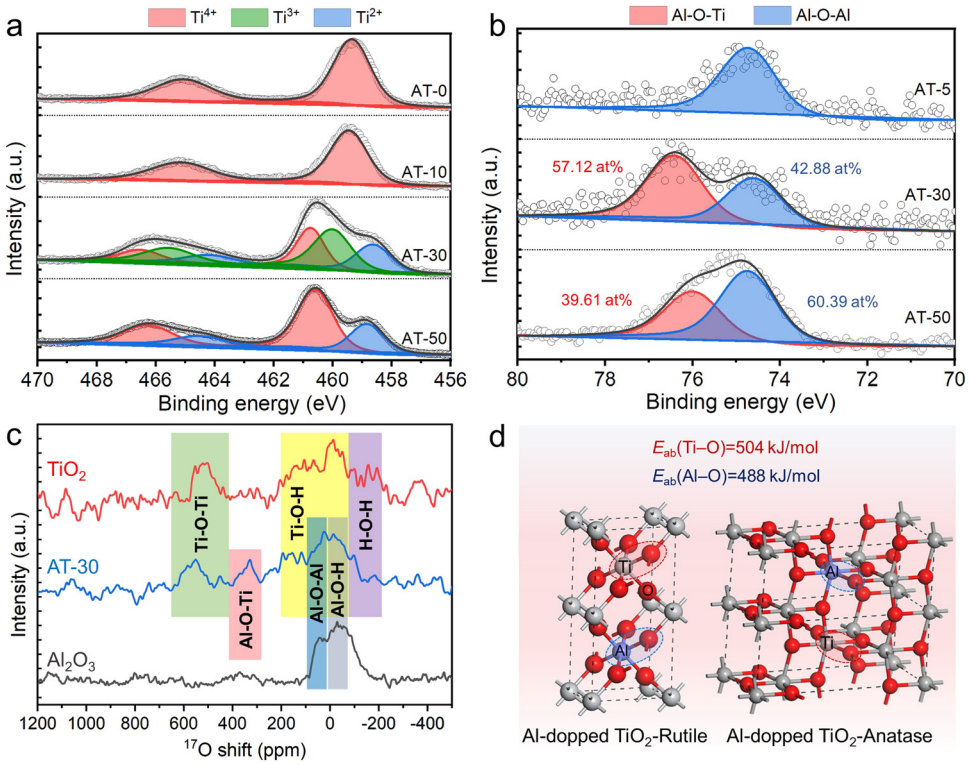

Fig. 3 (a and b) Ti 2p and Al 2p high-resolution XPS spectra obtained from AT-*n* nanofibers calcined at 900 °C. (c) Solid-state ^{17}O-NMR spectra of the AT-30, pure TiO_2, and Al_2O_3 nanofibers calcined at 900 °C. (d) Molecular structure of the Al-doped rutile and anatase TiO_2. Note that these structures are provided for the purpose of illustration but are not calculated structures.

the air) was dynamically monitored in a TEM chamber at temperatures ranging from 700 °C to 900 °C. The *in situ* heating temperature profile is supplemented in Fig. S8a (ESI†). Before heating, an amorphous shell with a maximum thickness of 17.2 nm, which was colored pink for distinction, was observed to be coated at the interfaces of TiO_2 nanocrystals (Fig. 4a). As discussed above, this amorphous shell should result from a segregation of Al_2O_3 and/or Al_2O_3–TiO_2 solid solution. When the heat treatment proceeded, the amorphous shell became densified and was segmented into small nanoparticles anchored to the grooves of neighboring TiO_2 nanocrystallites, finally generating a particle-on-fiber structure. Such a targeted location of Al_2O_3-based oxide could be ascribed to a low surface energy in the grooves of polycrystalline oxides.[15]

At the same time, the grain boundaries of TiO_2, marked by dashed lines, advanced faster as the amorphous shell became thinner (indicated by white arrows), suggesting accelerated sintering of TiO_2 nanocrystals. To quantitively estimate the thermodynamic driving force for the surface-initiated crystal growth,[28] the dihedral angle (γ) in the surface groove between TiO_2 crystals 1 and 2 was measured and tracked during the whole heating process. As plotted in Fig. S8b (ESI†), the presence of amorphous shells outside the TiO_2 nanocrystals helped retard the increase in the dihedral angle at high temperatures. A smaller dihedral angle in the surface groove provided a greater pinning effect for surface crystals to grow (*i.e.*, "drag" the grain boundary migration perpendicularly to the polycrystalline oxide surface). When the amorphous shell became thinner and even condensed into nanoparticles in the grooves of the grain boundaries, the dihedral angle started increasing in an accelerated fashion with an accelerated sintering rate.

Although there are some minor changes on the surface at high temperatures, the integrity of the TiO_2-based nanofibers is still remarkably impressive, indicating their superior sinter-resistance. As illustrated in Fig. 4b, the amorphous oxide homogeneously dispersed along the TiO_2 grain boundaries at a lower temperature, effectively hindering the advancement of grain boundaries and the sintering of TiO_2 nanocrystals upon heating. At an ultra-high temperature (>900 °C), the amorphous oxide is densified and then 'pinned' to the surface grooves of TiO_2 nanocrystals, repairing the surface defects and lowering the thermodynamic driving force for TiO_2 sintering.

In sharp contrast, severe densification can be visualized on pure TiO_2 nanofibers after heat-treatment at 700 °C for a short period of only 10 min (Fig. 4c and d). When the heating process proceeded, two neighboring TiO_2 nanocrystallites sintered rapidly into one with a larger size. The cracks, once initiated, immediately propagated in an unstable (often catastrophic) fashion on the prototypical strong yet brittle TiO_2 nanofibers. At 800 °C, the TiO_2 nanofiber suffered from catastrophic structure collapse and broke into two short nanorods (Video S5, ESI†). Hence, it is extremely obvious how crucial soft amorphous oxide is, for TiO_2 nanofibers, to maintain the

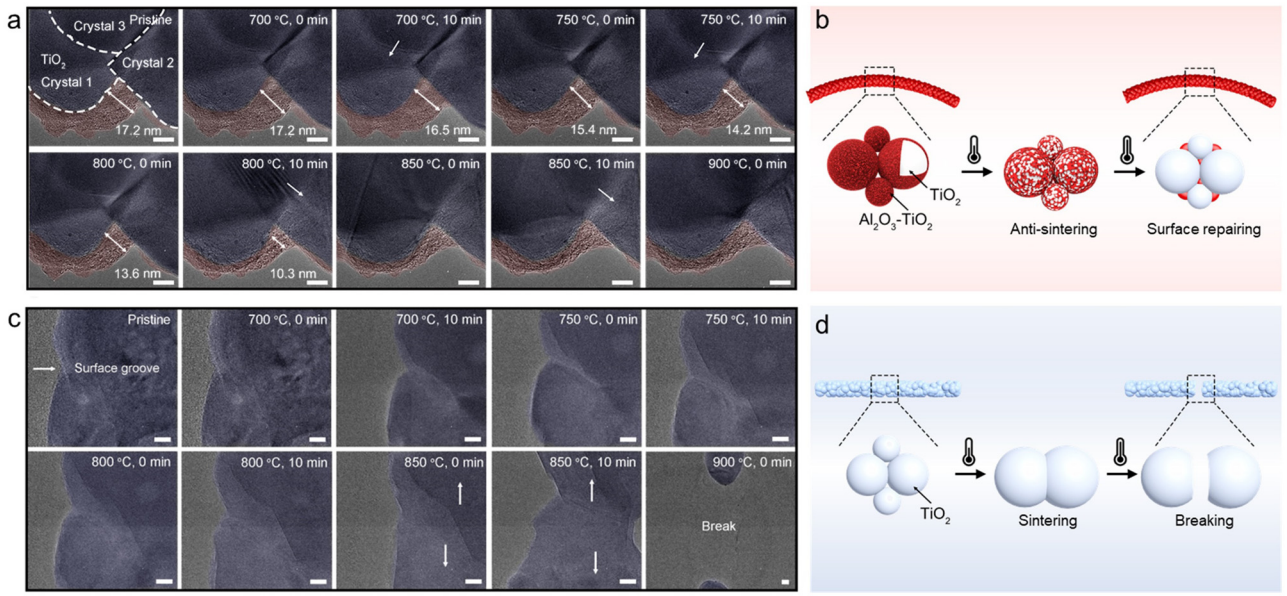

Fig. 4 Dynamic observation of the structural evolution at the TiO_2 grain boundaries at high temperatures. (a) Sequential TEM images of one AT-30 nanofiber pre-calcined at 700 °C under *in situ* heating, and (b) stabilizing mechanism of flexible-in-rigid AT nanofibers due to the inhibited crystal sintering. (c) Sequential TEM images of one unmodified TiO_2 nanofiber pre-calcined at 700 °C under *in situ* heating and (d) its breaking mechanism caused by the sintering of neighboring TiO_2 nanocrystals. The scale bars in a and c are 10 nm.

structural integrity under thermal stress and to optimize the flexibility of the resulting nanofibers.

Renewable air filters

Air pollution has long-lasting impacts on the atmospheric environment and public health. Specifically, $PM_{2.5}$, PM_{10}, and virus-containing particles can easily infiltrate into the human body, causing fatal and infectious diseases, such like lung cancer and the COVID-19 pandemic, and therefore worldwide social and economic disruption.[29] Electrospun nanofibers are widely used as efficient air filters, due to their high porosity, good interconnectivity, micrometer-sized interstitial space, and large surface-to-volume ratio.[14] Compared with the commonly used polymeric fibrous mats, oxide fibrous mats, if endowed with desirable mechanical performance, can serve as air filters particularly in harsh environments such as at extremely high temperatures, without the flammability issue. Moreover, the oxide fibrous mats also have the potential to degrade or decompose the contaminants, extending the lifespan of the filter and reducing the likelihood of producing secondary pollution, due to the photo- and/or thermo-catalytic activities of oxides.

Generally, the removal of submicron aerosol particles using fibrous mats is primarily based on the following mechanisms: Brownian diffusion, direct interception, inertial impaction, gravity, and chemical/physical attraction.[30] The naturally overlapping nanofibers with interconnected intra-fiber pores and channels facilitate the effective trapping for submicron aerosol particles. More importantly, the permanent dipole orientation and the trapping of adequate space charges, arising from the particle-on-fiber structure of the AT blended nanofibers, contributed to the remarkable filtration performance by enhancing long-range electrostatic interactions between the nanofibers and the pollutants.[30]

Herein, the filtration performance of TiO_2-based fibrous mats was quantitively evaluated by testing the removal efficiency of NaCl particles at room temperature. As shown in Fig. 5a, the filtration efficiencies for 2 μm-particulates under airflows of 32, 64, and 80 L min^{-1} on AT-30 mat were tested to be 96.31, 99.95, and 99.97%. The filtration efficiency of 99.97% meets the requirement of high efficiency particulate air (HEPA) filter standards,[31] and is competitive with that of various recently reported filters (Fig. 5b).[32–40] The corresponding pressure drops were 17, 30, and 48 Pa, respectively. On this basis, the quality factor (QF) could be calculated to be 0.15, 0.21, and 0.05, respectively. A better filter is one that possesses a higher filtration efficiency and/or lowers pressure drop, which corresponds to a higher QF value.

Moreover, incense smoke, which contains PM particles of various sizes, CO, CO_2, NO_2, SO_2, volatile organic compounds (VOCs), and other air pollutants,[27] was utilized to evaluate the high-temperature filtration efficiency. As known, many harmful particulate matter particles come from high-temperature gas (150–260 °C), such as automobile exhaust and industrial waste gas, extremely threatening the service life of the involved filters. By taking advantage of the superb thermal stability and flame retardancy, the TiO_2-based fibrous mats, as well as the fibrous sponge, a achieved filtration efficiency toward $PM_{2.5}$ and PM_{10} over 99.98% for at least 200 min (Fig. 5c). To be noted, the 3D sponge exhibited enhanced durability than that of two-dimensional (2D) mats after continuously filtering for 300 min, keeping a high filtration efficiency for $PM_{2.5}$ of 99.97% and PM_{10} of 99.99%. This could be ascribed to the ultrahigh porosity and ultralow packing density of the 3D fibrous sponges.

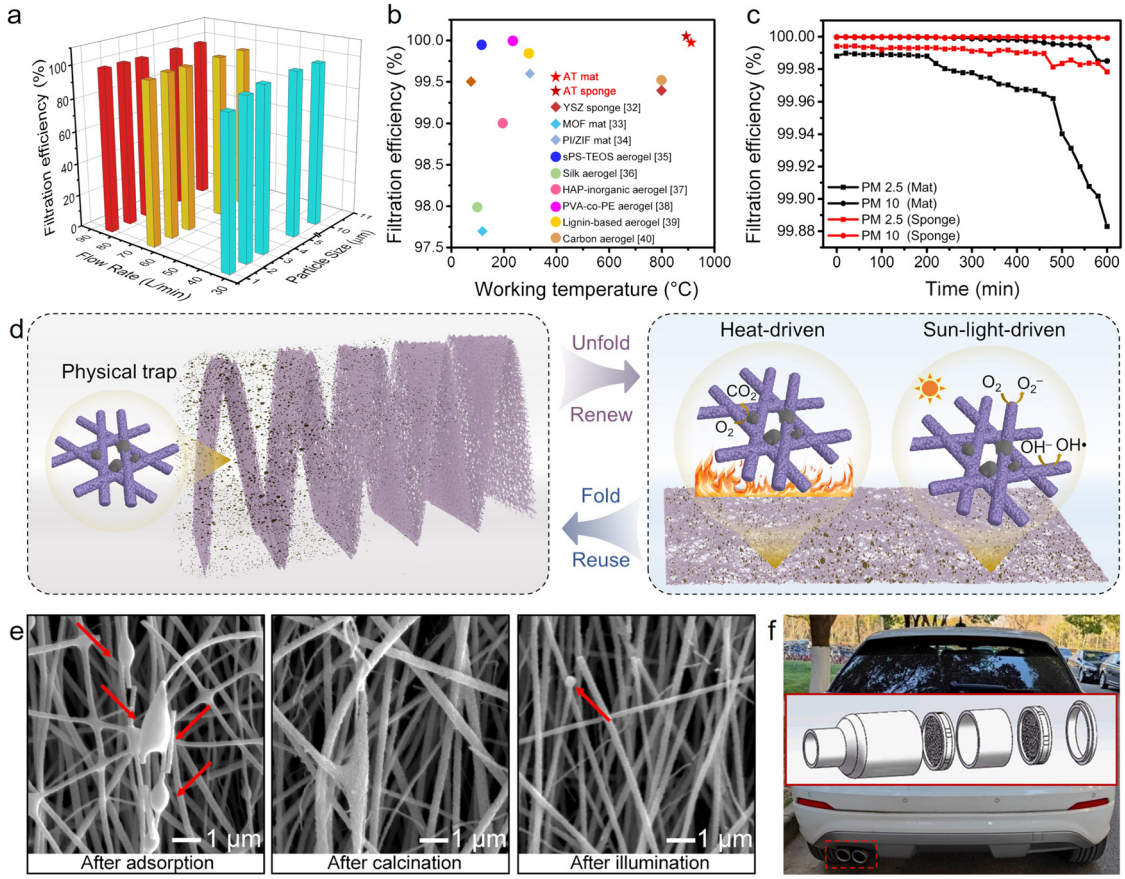

Fig. 5 Renewable air filter. (a) Filtration efficiency of an AT-30 fibrous mat. (b) Comparison of the filtration efficiency and the working temperature of our AT fibrous mat/sponge with those of other recently reported air filters. (c) Long-time filtration performance of AT fibrous mats and sponges. (d) Schematic of the renewable and high-temperature resistant air filter device. (e) SEM images of the AT-30 mat after filtrating burning incense, followed by a further regeneration by calcination at 500 °C or sunlight illumination for 4 h. The red arrow refers to the adsorbed flue gas particle. (f) Optical image and the object model diagram of a 3D printed automobile exhaust purifier.

The hierarchical pores and channels in the inter- and intra-nanofibers can provide longer residence time to ultrafine particles that undergo Brownian motion. The increase in filtration efficiency would only be accompanied by a small increase in pressure drop owing to the ultralow packing density and unique airflow regime of the 3D filters. Moreover, the slip flow of air molecules at the periphery of nanofibers becomes significant when the fiber diameter decreases to <500 nm,[29] which also helps to reduce the pressure drop.

As schemed in Fig. 5d, the 2D AT-30 mat could be engineered into a serpentine structure by origami technique to efficiently capture the PM particulates layer-by-layer. More excitingly, the folded filter could be unfolded, and further, be regenerated by *in situ* decomposing the captured PM particulates with the aid of light irradiation or heat treatment. As shown in the SEM images in Fig. 5e, the captured pollutants can be thermally decomposed by facile calcination in air at 500 °C, without destroying the oxide fibrous filter. Besides, the coexistence of anatase and rutile in the fibrous mat exhibited photocatalytic efficiency toward hazard degradation.[33] After being exposed to light irradiation for 4 h, the polluted filter can be regenerated in an environmental-friendly manner. After being equipped with an automobile exhaust purifier (inset in Fig. 5f) in the forms of layer-by-layer mats or sponges, the flexible-in-rigid nanofibers can facilitate the capture of high-temperature exhaust dust in a long term and minimize the unnecessary cost of filter replacement. This self-regenerative filtration system could work safely at harsh temperatures and potentially *in situ* capture and decompose the PM pollutants leveraging the burning heat, solving the PM pollution at its source.

Conclusions

In summary, we have demonstrated flexible-in-rigid TiO_2 nanofibers reinforced from a macro-scale to a molecular-scale. The doping of Al^{3+}-species into TiO_2 nanocrystals and the formation of an Al_2O_3–TiO_2 solid solution generated abundant flexible Ti–O–Al bonds, toughening the nanofibers on a molecular scale. The amorphous oxide at the TiO_2 grain boundaries restricted the coalescence of TiO_2 nanocrystals, and smartly filled the intergranular pores and the surface grooves. The resultant TiO_2-based nanofibers were endowed with an extremely

slender structure and therefore achieved a Young's modulus of 653.8 MPa and a tensile strength of 2.24 MPa. This free-standing TiO_2 fibrous mat can be easily constructed into a sponge with a density as low as 22 mg cm^{-3}, using a simple origami craft. The folded fibrous sponges achieved 99.99% filtration efficiency toward PM_{10} after working for 300 min, and could be regenerated by calcination or sunlight irradiation due to their (photo)catalytic activity inherited from their anatase/rutile mixture nature. This work sheds light on scaling-up the production of flexible TiO_2 nanofibers, which represent an attractive fibrous material with functional and mechanical capability.

Author contributions

W. F. synthesized and characterized most of the nanofibers, analyzed the data, and wrote and revised the manuscript. W. X. synthesized and characterized part of the samples, analyzed the part of the stress distribution simulation, estimated air-purification performance, and wrote the manuscript draft. K. Y. performed the *in situ* TEM experiments and revised the *in situ* observation part. X. M. carried out part of the mechanical test. Y. W. and L. P. contributed to the solid-state ^{17}O-NMR characterization and analysis. M. T. conducted HAADF-STEM observation. L. S. and Y. S. revised the manuscript. Y. D. conceived the idea and revised the manuscript. All authors read the manuscript and approved the submitted version.

Conflicts of interest

There are no conflicts to declare.

Acknowledgements

This work is especially for the 120th anniversary of Southeast University and was financially supported by the National Natural Science Foundation of China (21975042, 12174050, 21972066), the National Key R&D Program of China (no. 2020YFC1511902), the Innovation Platform Project Supported by Jiangsu Province (6907041203), the open project of the State Key Laboratory of Physical Chemistry of Solid Surfaces in Xiamen University, and the Postdoctoral Research Start-Up Fund in Southeast University.

References

1 Q. Liu, D. Zhai, Z. Xiao, C. Tang, Q. Sun, C. R. Bowen, H. Luo and D. Zhang, *Nano Energy*, 2022, **92**, 106702.
2 N. Feng, H. Lin, H. Song, L. Yang, D. Tang, F. Deng and J. Ye, *Nat. Commun.*, 2021, **12**, 4652.
3 E. Wierzbicka, T. Schultz, K. Syrek, G. D. Sulka, N. Koch and N. Pinna, *Mater. Horiz.*, 2022, **9**, 2797–2808.
4 M. Kim, I. Choi, S. J. Choi, J. W. Song, S. I. Mo, J. H. An, Y. Jo, S. Ahn, S. K. Ahn, G. H. Kim and D. S. Kim, *Joule*, 2021, **5**, 659–672.
5 Grand View Research, Inc, Titanium dioxide market size, share & trends analysis report by grade (anatase, rutile), by production process (sulfate, chloride), by application (paints & coatings, plastics), by region, and segment forecasts, 2021-2028, **https://www.grandviewresearch.com**, accessed: 03, 2022.
6 M. Ge, C. Cao, J. Huang, S. Li, Z. Chen, K. Q. Zhang, S. S. Al-Deyab and Y. Lai, *J. Mater. Chem. A*, 2016, **4**, 6772.
7 D. Li and Y. Xia, *Nano Lett.*, 2003, **3**, 555–560.
8 F. Xu, J. Zhang, B. Zhu, J. Yu and J. Xu, *Appl. Catal., B*, 2018, **230**, 194–202.
9 B. Fu, J. Li, H. Jiang, X. He, Y. Ma, J. Wang and C. Hu, *Nano Energy*, 2022, **93**, 106841.
10 L. Yao, W. Pan, J. Luo, X. Zhao, J. Cheng and H. Nishijima, *Nano Lett.*, 2018, **18**, 130–136.
11 H. Ping, W. Wagermaier, N. Horbelt, E. Scoppola, C. Li, P. Werner, Z. Fu and P. Fratzl, *Science*, 2022, **376**, 188–192.
12 C. Liu, S. Wang, N. Wang, J. Yu, Y. T. Liu and B. Ding, *Nano-Micro Lett.*, 2022, **14**, 194.
13 J. Guo, S. Fu, Y. Deng, X. Xu, S. Laima, D. Liu, P. Zhang, J. Zhou, H. Zhao, H. Yu, S. Dang, J. Zhang, Y. Zhao, H. Li and X. Duan, *Nature*, 2022, **606**, 909–915.
14 J. Xue, T. Wu, Y. Dai and Y. Xia, *Chem. Rev.*, 2019, **119**, 5298–5415.
15 Y. Yang, A. Kushima, W. Han, H. Xin and J. Li, *Nano Lett.*, 2018, **18**, 2492–2497.
16 H. Wang, X. Zhang, N. Wang, Y. Li, X. Feng, Y. Huang, C. Zhao, Z. Liu, M. Fang, G. Ou, H. Gao, X. Li and H. Wu, *Sci. Adv.*, 2017, **3**, e1603170.
17 J. Song, X. Wang, J. Yan, J. Yu, G. Sun and B. Ding, *Sci. Rep.*, 2017, **7**, 1636.
18 J. Song, X. Wu, M. Zhang, C. Liu, J. Yu, G. Sun, Y. Si and B. Ding, *Chem. Eng. J.*, 2020, **379**, 122269.
19 Y. Wang, W. Li, Y. Xia, X. Jiao and D. Chen, *J. Mater. Chem. A*, 2014, **2**, 15124.
20 Y. Xie, L. Wang, B. Liu, L. Zhu, S. Shi and X. Wang, *Mater. Des.*, 2018, **160**, 918–925.
21 Z. Liu, Y. Tang, K. Zhao and W. Chen, *Appl. Surf. Sci.*, 2019, **489**, 717–724.
22 Y. Si, X. Tang, J. Ge, S. Yang, M. El-Newehy, S. S. Al-Deyab, J. Yu and B. Ding, *Nanoscale*, 2014, **6**, 2102–2105.
23 S. Arabha, A. H. Akbarzadeh and A. Rajabpour, *Composites, Part B*, 2020, **200**, 108260.
24 S. Wu, Z. Kou, Q. Lai, S. Lan, S. S. Katnagallu, H. Hahn, S. Taheriniya, G. Wilde, H. Gleiter and T. Feng, *Nat. Commun.*, 2022, **13**, 5468.
25 A. L. Patterson, *Phys. Rev.*, 1939, **56**, 978–982.
26 D. Padayachee, A. S. Mahomed, S. Singh and H. B. Friedrich, *ACS Catal.*, 2020, **10**, 2211–2220.
27 J. He and T. Kunitake, *Soft Matter*, 2006, **2**, 119–125.
28 J. A. Segre, *Science*, 2015, **349**, 1058–1059.
29 R. Yang, Y. Fan, R. Ye, X. Tang, X. Cao, Z. Yin and Z. Zeng, *Adv. Mater.*, 2021, **33**, 2004862.
30 C. Liu, P. C. Hsu, H. W. Lee, M. Ye, G. Zheng, N. Liu, W. Li and Y. Cui, *Nat. Commun.*, 2015, **6**, 6205.
31 US Dept. of Defense. Mil-Std-282: department of defense test method standard. Washington 25 D.C. (1956).

32 H. Wang, S. Lin, S. Yang, X. Yang, J. Song, D. Wang, H. Wang, Z. Liu, B. Li, M. Fang, N. Wang and H. Wu, *Small*, 2018, **14**, 1800258.
33 P. Li, J. Li, X. Feng, J. Li, Y. Hao, J. Zhang, H. Wang, A. Yin, J. Zhou, X. Ma and B. Wang, *Nat. Commun.*, 2019, **10**, 2177.
34 Z. Hao, J. Wu, C. Wang and J. Liu, *ACS Appl. Mater. Interfaces*, 2019, **11**, 11904–11909.
35 S. J. Kim, G. Chase and S. C. Jana, *Sep. Purif. Technol.*, 2016, **166**, 48–54.
36 Z. Hu, S. Yan, X. Li, R. You, Q. Zhang and D. L. Kaplan, *ACS Nano*, 2021, **15**, 8171–8183.
37 Y. G. Zhang, Y. J. Zhu, Z. C. Xiong, J. Wu and F. Chen, *ACS Appl. Mater. Interfaces*, 2018, **10**, 13019–13027.
38 Q. Liu, J. Chen, T. Mei, X. He, W. Zhong, K. Liu, W. Wang, Y. Wang, M. Li and D. Wang, *J. Mater. Chem. A*, 2018, **6**, 3692–3704.
39 Z. Zeng, X. Y. D. Ma, Y. Zhang, Z. Wang, B. F. Ng, M. P. Wan and X. Lu, *ACS Sustainable Chem. Eng.*, 2019, **7**, 6959–6968.
40 C. Ding, Y. Liu, P. Xie, J. Lan, Y. Yu, X. Fu, X. Yang and W. H. Zhong, *J. Mater. Chem. A*, 2021, **9**, 13143–13150.

